Influence of high-temperature chemical non-equilibrium and surface micropore effect on boundary layer stability*

WEN Jinghao[1], LI Chenhui[1, 2], TU Guohua[1, *], WAN Bingbing[1, *], DUAN Maochang[1], ZHANG Rui[1]

1. State Key Laboratory of Aerodynamics, Mianyang 621000, China
2. School of Aeronautic Science and Engineering, Beihang University, Beijing 100191, China

Abstract

The transition from laminar to turbulent flow is one of the main aerodynamic challenges in aircraft design and development. When the flight Mach number is sufficiently high, the aircraft surface undergoes micropore effects and high-temperature gas thermochemical reactions. At present, boundary layer instability has become a more complex problem, and its mechanism is still unclear. In this study, a linear stability analysis method is developed which takes into consideration high-temperature chemical non-equilibrium process and surface micropore effect. For flight conditions at high altitude (H = 25 km) with Mach numbers 10, 15, and 20, the effects of micropore effects, chemical non-equilibrium effects, and their joint effect on flow stability are contrasted and investigated. The results show that the chemical non-equilibrium effect can promote the boundary layer's mode instability, while the micropore effect can restrain the second mode instability. The coexistence of the two often contributes to the instability of the second mode, because the former is more significant than the latter. The chemical non-equilibrium effect can reduce the frequency range corresponding to the second mode of pore effect inhibition, which results in the chemical non-equilibrium effect enhancing the inhibition effect of the micropore effect in the local low-frequency range and weakening its inhibition effect in the high-frequency range. This, in turn, causes a decrease in the

* The paper is an English translated version of the original Chinese paper published in Acta Physica Sinica. Please cite the paper as: WEN Jinghao, LI Chenhui, TU Guohua, WAN Bingbing, DUAN Maochang, ZHANG Rui，**Influence of high-temperature chemical non-equilibrium and surface micropore effect on boundary layer stability**. *Acta Phys. Sin.*, 2025, 74(12): 124701. doi: 10.7498/aps.74.20250269

corresponding *N* value variation by pore effect. Furthermore, when both effects are present, the micropore effect's capacity to inhibit the second mode is not significantly affected by change in Mach number.

Keywords: boundary layer; stability; chemical non-equilibrium; micropore effect
PACS: 47.15.Fe; 47.70.Fw; 47.85.L-
doi: 10.7498/aps.74.20250269
cstr: 32037.14.aps.74.20250269

1. Introduction

The transition from laminar to turbulent boundary layer is a complex process with multi-factor coupling, which is an important research direction in the field of aerodynamics[1]. In practical applications, the heat flux and friction in turbulent state after boundary layer transition are 3-5 times higher than those in laminar state, so transition is an important consideration in aircraft aerodynamic design, and it is also one of the most challenging basic scientific problems restricting the development of advanced aircraft[2].

In general, natural transition is dominated by boundary layer mode instability. In the high speed field, if the temperature in the flow is insufficient to alter the specific heat capacity of the gas, the gas still satisfies the ideal gas equation of state, which is called calorimetric perfect gas (CPG). In this state, the two-dimensional boundary layer is usually dominated by Mack mode instability. When the temperature in the boundary layer is high enough at high Mach number, a series of thermochemical reactions will occur in the surface gas, which will significantly change the flow characteristics in the boundary layer, thus affecting the modal instability process. According to whether the thermochemical reaction process is in equilibrium or not[3,4], the flow can be divided into thermochemical frozen(TCF), thermochemical equilibrium (TCE), thermochemical non-equilibrium (TCNE) and chemical non-equilibrium (CNE).

For the flow considering the thermochemical reaction process, the streamwise instability is still dominated by the Mack mode, and the related research has been carried out as early as the 1990s. Malik et al.[5] studied the flow stability considering the high temperature real gas effect earlier, and found that the thermochemical equilibrium would make the second mode more unstable, but it would stabilize the first mode. Stuckert and Reed's study on chemical non-equilibrium flow[6] also reached the same conclusion. In addition, the thermochemical non-equilibrium flow and the chemical non-equilibrium flow are compared, and the results show that the vibrational non-equilibrium has a stabilizing effect on the second mode[7,8]. For the higher frequency unstable modes, Chen et

al.[9] found an obvious third mode in the thermochemical non-equilibrium flow over a blunt cone at Mach 20, but its growth rate did not exceed that of the second mode. Under the same gas model, Zhao Zhouyuan et al. used LPSE to study the effect of wall temperature in wedge flow. The lower the wall temperature is, the later the disturbance with the same frequency develops along the streamwise direction, but the maximum *N* value at downstream increases. In addition, because the simulation of high temperature non-equilibrium flow requires the use of appropriate models to characterize the physical and chemical properties[11] of each component, scholars have explored the effects of different thermodynamic models[12,13], diffusion models[14-16], transport models[12,17-21], chemical reaction models[22-24] and wall catalytic effects[25] on the stability of the boundary layer, which will not be expanded here.

Aircraft in high-speed flight are faced with harsh aerodynamic and thermal environments, which put forward higher requirements for thermal protection system design and material performance, while the maximum temperature of existing ultra-high temperature materials does not exceed 3000 K[26]. In order to reduce the design difficulty of the thermal protection system and improve the range, many researchers use active/passive means to control the boundary layer transition. Porous materials applied to the outer surface of aircraft can absorb high-frequency sound waves and suppress the second mode, which can be used as an effective method of passive transition control[27]. In the calorimetric perfect gas state, there are abundant studies on how the pore effect affects the instability of the boundary layer. Fedorov and Malmuth[28] and Zhao et al.[29] respectively derived the effective mobility model reflecting the pore effect, and the latter model takes into account the higher-order diffraction modes. Fedorov and Malmuth[28] explored the effect of holes on the stability of boundary layer on a flat plate by using the linear stability (LST) method considering the pore effect. The results show that the pore effect reduces the growth rate of the second mode, but slightly promotes the growth rate of the first mode. Wartemann et al.[30] and Xu et al.[31] obtained the same conclusion. Wang and Zhong[32] explored the mechanism of the effect of the local porous coating on the high-speed boundary layer experimentally and numerically, and found that the control effect of the local porous coating was closely related to the synchronization process of the fast and slow modes in the boundary layer. If the porous coating is placed downstream of the synchronization point, the second mode can be significantly suppressed, but the mode growth can be promoted when it is put upstream. The experimental results of Rasheed et al.[33] and Lukashevich et al.[34] are consistent with this conclusion. Using direct numerical simulation (DNS), Guo Qilong et al. [35] investigated the effect of millimeter-scale microgrooves on the second mode disturbances. They discovered that the microgrooves can suppress the second mode in a wide frequency range, and that the suppression effect grows as the grooving ratio increases. Liu Yong et

al.[36] further studied the microgroove with the same size, and the results showed that when the microgroove was set in the maximum growth rate interval or near the synchronization center of the fast/slow mode, the disturbance suppression of the second mode was the most significant. The wind tunnel experimental results of Gui et al.[37] also show that the porous coating can suppress the second mode, and the modal nonlinearity of the porous wall is much weaker than that of the smooth wall. It is also found that the growth rates of the instability modes calculated by LST with the effect of a regular circular hole are in good agreement with the experiments. Liu et al.[38] explored the effect of porous coupled micro-blowing and suction on the stability of Mach 6 boundary layer. When the blowing and suction point is located upstream of the synchronization point of the second mode, it is found that the porous structure is helpful to suppress high-frequency disturbances. If the blowing-suction point is located in the region dominated by the dominant mode, the porous structure will prematurely excite the low-frequency unstable mode.

The above study on the influence of pore effect on the instability of boundary layer flow is based on the calorimetric perfect gas model. At present, there are few studies on the application of micropore structure in high temperature chemical non-equilibrium flow. When Wang and Zhong[39] studied the difference between calorimetric perfect gas and thermochemical non-equilibrium flow, they carried out a preliminary numerical simulation study on this issue. It was found that the boundary layer disturbance wave excited by wall blowing and suction in calorimetry perfect gas state would be significantly suppressed by regular porous coating. Subsequently, Wang[40] et al. Further compared the pressure fluctuation amplitude on the flat plate wall at Mach number 10, and found that for the dominant second mode disturbance (frequency 300 and 400 kHz), the thermochemical non-equilibrium effect can enhance the suppression effect of the porous coating, but the study did not compare the LST and DNS results for the porous wall under the TCNE assumption. Ken et al.[41] added Fedorov's porous admittance model to LST considering thermochemical non-equilibrium effects. Through DNS, it is found that the distribution of dimensionless wall pressure fluctuation along the streamwise direction is consistent under the CPG and TCNE assumptions, which is due to the small effect of TCNE on the attenuation of unstable disturbances in the microporous cavity. The study also compared the LST and DNS results of the porous wall at the same frequency under the TCNE condition, and proved that if the porous coating region is long enough, the use of the wall admittance model in the LST can well predict the trend of disturbance growth in the DNS. However, this work has not further studied the influence of microporosity effect on different frequency disturbance and *N* value under high temperature gas model.

In general, the understanding of boundary layer instability considering the combined effect of chemical non-equilibrium and surface porosity remains insufficient, and its influence mechanism is not clear enough, so the study of boundary layer instability under the two effects needs to be further carried out. In this paper, a linear stability theory which can reflect the chemical non-equilibrium effect and micropore effect at high temperature is established, and the instability mechanism of the high-speed boundary layer with chemical non-equilibrium, micropore and their coexistence is explored. The effects of Mach number and micropore geometry on the stability are also investigated.

2. Research method

In this paper, a boundary layer flow stability analysis method which takes into account the effects of high temperature chemical non-equilibrium and porous effects is established. Firstly, the flow control equation of high temperature chemical nonequilibrium and the linear stability equation are derived, and then the porous mobility model is added to the wall boundary condition of the stability equation to establish the flow stability analysis method considering the above two effects.

2.1 Governing equation of flow

For the problem of high temperature chemical non-equilibrium flow, the two-dimensional Navier-Stokes equations are constructed, and their conservative expressions are as follows[25]

$$\frac{\partial \rho}{\partial t} + \frac{\partial (\rho u_j)}{\partial x_j} = 0, \tag{1}$$

$$\frac{\partial (\rho u_i)}{\partial t} + \frac{\partial (\rho u_i u_j)}{\partial x_j} = -\frac{\partial (\delta_{ij} p)}{\partial x_j} + \frac{\partial \tau_{ij}}{\partial x_j}, \tag{2}$$

$$\begin{aligned} &\frac{\partial (\rho E)}{\partial t} + \frac{\partial (\rho H u_j)}{\partial x_j} \\ = \ &\frac{\partial}{\partial x_j}\left(\tau_{ij} u_i + \lambda \frac{\partial T}{\partial x_j} + \sum_{s=1}^{ns} \rho D_s h_s \frac{\partial Y_s}{\partial x_j}\right), \end{aligned} \tag{3}$$

$$\frac{\partial (\rho Y_s)}{\partial t} + \frac{\partial}{\partial x_j}(\rho Y_s u_j) = \frac{\partial}{\partial x_j}\left(\rho D_s \frac{\partial Y_s}{\partial x_j}\right) + \dot{\omega}_s. \tag{4}$$

The conservation equations for mass, momentum, total energy, and species are (1) through (4). Here, ρ,u_i,p,T and Y_s denote density, velocity components, pressure,

temperature, and species mass fraction, respectively. H is total specific enthalpy and E is total specific energy. λ, D_s, h_s and ω_s are thermal conductivity, component diffusivity, component specific enthalpy and component mass formation rate. τ_{ij} is the viscous shear stress tensor. The subscript i or j indicates the velocity component, and the subscript s represents the number of components.

In this study, a 5-component model of air (corresponding to N_2, O_2, N, O, NO, $ns = 5$) was used to simulate the reacting flow, and the incoming gas components were O_2 and N_2 with mass fractions of 22% and 78%. Respectively. Thermodynamic parameters (such as specific heat and specific enthalpy) of single component were calculated by CHEMKIN fitting[13]. Viscosity coefficient, thermal conductivity coefficient and mass diffusivity coefficient were calculated by Blottner fitting[18], Eucken empirical[42] and constant Schmidt number diffusion model[43]. The transport coefficient of air mixture is calculated by Wilke's mixture law[44].

2.2 Linear stability theory

In this study, the LST code considering chemical non-equilibrium effects is used to analyze the reacting flow, and the traditional LST method[45] is used to analyze the calorimetrical perfect gas flow. In this paper, the framework of linear stability theory based on chemical nonequilibrium effects is presented[25]. In the stability theory, the physical quantity $\boldsymbol{q} = [\rho, u, v, w, T, Y_s]^{\mathrm{T}}, s = 1,2,3,4$ can be expressed as the basic quantity $\boldsymbol{q}_0$ and the disturbance quantity $\boldsymbol{q}'$, where u denotes the streamwise velocity. The normal velocity is denoted by v. The spanwise velocity is denoted by w. Since both the basic quantity and the perturbed quantity satisfy Equation (1) - Equation (4), the equation set satisfied by the perturbed quantity can be obtained by substitution and subtraction in the equation:

$$\begin{aligned} &\boldsymbol{F}\frac{\partial \boldsymbol{q}'}{\partial t} + \boldsymbol{A}\frac{\partial \boldsymbol{q}'}{\partial x} + \boldsymbol{B}\frac{\partial \boldsymbol{q}'}{\partial y} + \boldsymbol{C}\frac{\partial \boldsymbol{q}'}{\partial z} + \boldsymbol{D}\boldsymbol{q}' \\ &+\boldsymbol{V}_{xx}\frac{\partial^2 \boldsymbol{q}'}{\partial x^2} + \boldsymbol{V}_{yy}\frac{\partial^2 \boldsymbol{q}'}{\partial y^2} + \boldsymbol{V}_{zz}\frac{\partial^2 \boldsymbol{q}'}{\partial z^2} \\ &+\boldsymbol{V}_{xy}\frac{\partial^2 \boldsymbol{q}'}{\partial x\,\partial y} + \boldsymbol{V}_{yz}\frac{\partial^2 \boldsymbol{q}'}{\partial y\,\partial z} + \boldsymbol{V}_{xz}\frac{\partial^2 \boldsymbol{q}'}{\partial x\,\partial z} = \boldsymbol{N}, \end{aligned} \tag{5}$$

In the equation, the matrix $\boldsymbol{F}$,$\boldsymbol{A}$,$\boldsymbol{B}$,$\boldsymbol{C}$,$\boldsymbol{D}$ and $\boldsymbol{V}$ are increased from 5 × 5 in the calorimetric perfect gas model to 9 × 9 in the chemical non-equilibrium gas model (with additional component terms), and the coefficients in the matrix are only related to the basic flow. $\boldsymbol{N}$ represents the nonlinear term, which is ignored in the linear stability analysis.

Assuming that the flow satisfies the local parallel condition, the solution of the perturbation equation can be expressed as

$$q' = \hat{q}(y)\exp\left[\mathrm{i}(\alpha x + \beta z - \omega t)\right], \qquad (6)$$

Here $\hat{q}(y)$ denotes the perturbed shape function and is a function of the normal coordinate y. In the spatial mode, the ω is a real number and represents the frequency of the wave. At least one of α and β is complex, the real parts represent the streamwise and spanwise wavenumbers, while the imaginary part represents the growth rate. For two-dimensional waves, there are $\beta = 0$. Substituting (6) into equation (5) and neglecting higher order terms and nonlinear terms, the linear stability equation is derived, and the first-order differential equation is as follows:

$$\mathrm{d}\hat{\boldsymbol{\Phi}}/\mathrm{d}y = \boldsymbol{A}_0\hat{\boldsymbol{\Phi}}, \qquad (7)$$

The coefficient of matrix $\boldsymbol{A}_0$ is increased from 8 × 8 of calorimetric perfect gas model to 16 × 16 of chemical non-equilibrium gas model, and the $\hat{\boldsymbol{\Phi}}$ is a vector composed of 16 perturbations. For the equation (7), the Malik two-point fourth-order compact difference method is used to solve it, and the eigenvalues of the unstable modes are obtained.

2.3 Porous model and boundary condition

The micro porous structure of the wall will interfere with the disturbance wave in the boundary layer, and the wall disturbance is no longer zero. In general, the key parameters to be considered for regular porous walls include half-width or radius b, pore depth H, periodic width s and porosity n, which is equal to “pore surface area/total surface area of open pore area”. A simple configuration of periodically distributed microgrooves and circular holes is shown in Fig. 1, which satisfies the assumption of infinite length in the spanwise direction.

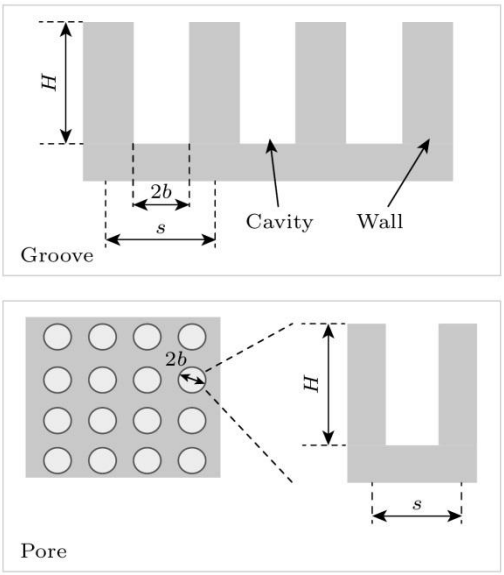

Figure 1. Schematic diagram of a simple cross-section.

When the periodic spacing s of the hole is much smaller than the boundary layer thickness, the effect of the hole wall on the basic flow field of the boundary layer can be neglected[46,47], so only the porous effect is considered in the stability equation. At the same time, considering the multi-component gas boundary of high temperature chemical non-equilibrium effect, assuming that the normal gradient of each component gas mass fraction is zero. The high temperature chemical non-equilibrium flow boundary condition on the porous wall is expressed as

$$\hat{u} = \hat{w} = 0, \hat{v} = A\hat{p}, \hat{T} = B\hat{p}, \frac{\mathrm{d}Y_s}{\mathrm{d}y} = 0 \qquad (8)$$

Where *A* and *B* are acoustic admittance and thermal admittance, respectively, but the influence of thermal admittance is generally very small[48], and the influence of admittance *A* is mainly considered in the following studies. The Mack mode instability wave is simplified to normal incidence, and the effective admittance can be expressed by assuming that the period width *s* is much smaller than the incident wavelength λ_{acs}.

$$A = \frac{\hat{v}}{\hat{p}}|_{\mathrm{w}} = \frac{1}{\rho_{\mathrm{w}} c_{\mathrm{w}}} \frac{R_0 - 1}{R_0 + 1} \qquad (9)$$

Here ρ_{w} and c_{w} are the wall density and sound velocity. When the s is much smaller than the λ_{acs} of the incident wavelength, the high-order diffraction modes cannot radiate to the far field[29], and the specular reflection is mainly considered. The R_0 is the reflection coefficient. For two-dimensional waves, the specific expression is as follows:

$$R_0 = 1 + \frac{2\mathrm{j}\tan(k_\mathrm{c}H)n(\rho_\mathrm{w}/\tilde{\rho})(k_\mathrm{c}/k_0)}{1-\mathrm{j}\tan(k_\mathrm{c}H)n(\rho_\mathrm{w}/\tilde{\rho})\sum_{r=-\infty}^{+\infty} k_\mathrm{c}S_r^2/k_y^{(r)}} \quad (10)$$

The vertical and harmonic quantities of the reflected wave of order *r* are $k_y^{(r)} = \sqrt{k_0^2 - (k_x^{(r)})^2}$, $k_x^{(r)} = k_x + 2\pi r/s$, respectively, and the wavenumber is $k_0 = \omega/c_\mathrm{w}$, Both the effective density $\tilde{\rho}$ and the wavenumber k_c = are complex parameters related to the frequency ω, which are specifically defined as

$$\tilde{\rho} = \rho_\mathrm{w}/\psi_\mathrm{v}, k_\mathrm{c} = \sqrt{k_0^2 \frac{\gamma-(\gamma-1)\psi_\mathrm{t}}{\psi_\mathrm{v}}} \quad (11)$$

For regular micropores:

$$\psi_i = \frac{\mathrm{J}_2(bk_i)}{\mathrm{J}_0(bk_i)}, i = \mathrm{t,v}, S_r = \frac{2\mathrm{J}_1(bk_x^{(r)})}{bk_x^{(r)}} \quad (12)$$

Where the viscous wave number is $k_\mathrm{v} = \sqrt{\mathrm{j}\omega\rho_\mathrm{w}/\mu}$ and the thermal wave number is $k_\mathrm{t} = \sqrt{\mathrm{j}\omega\rho_\mathrm{w}C_\mathrm{p}/\kappa}$, μ, C_p and κ are the viscosity coefficient, the specific heat at constant pressure and the heat conduction coefficient, respectively. $\mathrm{J}_0(\cdot)$, $\mathrm{J}_1(\cdot)$ and $\mathrm{J}_2(\cdot)$are the zero-order, first-order and second-order forms of the Bessel function of the first kind.

For two-dimensional microgrooves:

$$\psi_i = 1 - \tan(bk_i), i = \mathrm{t,v}, S_r = \mathrm{sinc}(bk_x^{(r)}) \quad (13)$$

The remaining parameters in the equation (10)-(13) are consistent with those defined in refenerces [29,49].

2.4 Verification result

2.4.1 Program verification

The basic flow field in the study is calculated by the CFD software NNW-HyFLOW of the National Numerical Wind Tunnel Project. The flow field is solved by the AUSMPW + scheme with second-order upwind interpolation and the Minmod limiter to calculate the spatial convective flux. The viscous term is calculated by the central scheme and iterated by the LU-SGS implicit time marching method. Firstly, the reliability of the software is

verified by the calorimetric perfect gas (CPG) model and the chemical non-equilibrium (CNE) gas model. For the former, the selected verification example is the adiabatic flat plate boundary layer of Kline[50]: incoming flow Mach number Ma = 10, incoming flow temperature T_∞ = 350 K, Reynolds number Re = 6.0 × 10^6 m^{-1}, and the verification results compared with the literature are shown in Fig. 2. For the latter, the verification example is the chemical non-equilibrium adiabatic flat plate boundary layer of Miró Miró[51]: the incoming flow Mach number and unit Reynolds number are consistent with the setting of Kline, and the incoming flow temperature T_∞ = 600 K. The verification results are compared with literature data in Fig. 3. From the comparison results of Fig. 2 and Fig. 3, it is feasible to use HyFLOW to simulate the basic flow field in the study. Unless otherwise specified, the dimensionless reference length in this paper is L_{ref} = 1 mm.

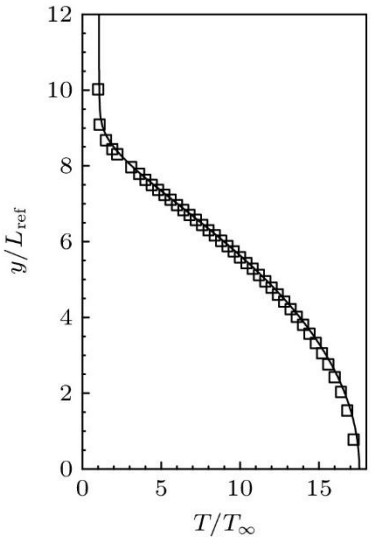

Figure 2. Temperature profile comparison under CPG circumstance at x/L_{ref} = 600.

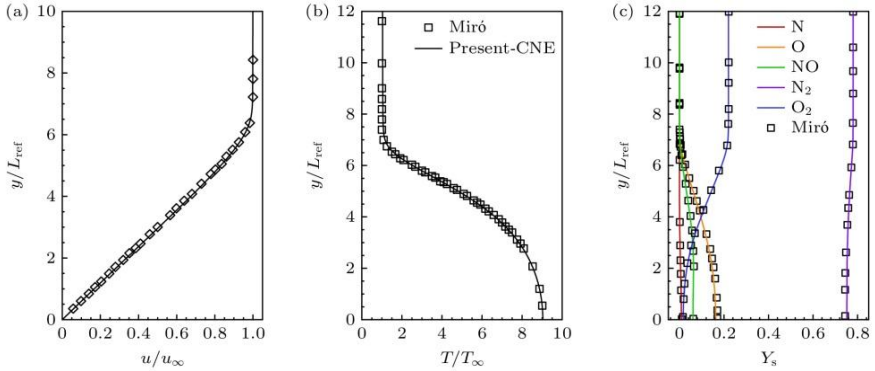

Figure 3. Baisc flow profiles at x/L_{ref} = 600 under CNE circumstance: (a) Streamwise velocity; (b) temperature; (c) species concentration.

To verify the effectiveness of the stability analysis method considering the porous effect, an example of the stability analysis of the porous wall under the calorimetric perfect gas model is given as follows: Reynolds number Re = 1.0 × 10^7 m^{-1}, inflow temperature T_∞ = 216.65 K, and the wall is an adiabatic wall. The parameters of the circular hole in the

porous wall are as follows: n = 0.25, h = 2 mm, b = 0.09375 mm. The shape function and growth rate of Mack mode under smooth/porous wall given by Fig. 4 are compared with the results of Wartemann et al.[30] and Luedeke et al.[48]. The adiabatic wall temperature at the streamwise position is T_w = 1522.44 K. The consistency of the two results verifies the reliability of the LST code in this paper to analyze the porous effect.

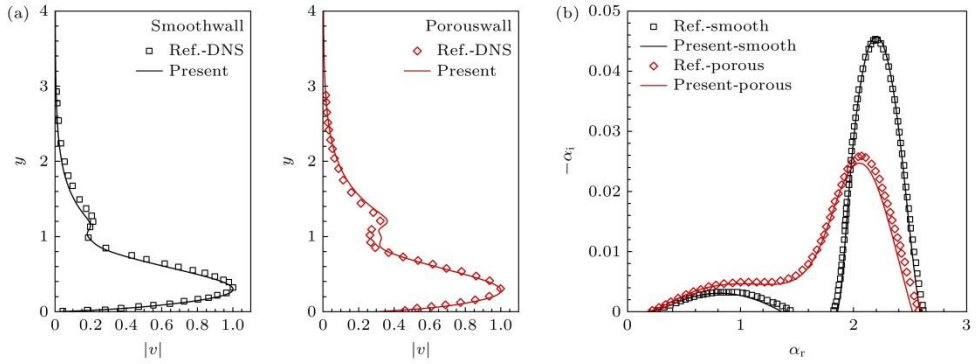

Figure 4. Comparison of literature and present results: (a) Eigenfunction; (b) growth rate.

2.4.2 Mesh independence verification

In this paper, the atmospheric parameters are selected at the height of H = 25 km, and the calorimetric perfect gas (CPG) and chemical non-equilibrium (CNE) gas models are used for calculation respectively. The wall condition for basic flow calculation is adiabatic wall, and the specific parameters are listed in Tab. 1. The ρ_∞ and U_∞ are the incoming flow density and velocity.

Table 1. Flow characteristics for various Mach numbers.

Ma	T_∞/K	ρ_∞/(kg·m^{-3})	U_∞/(m·s^{-1})	Re/m^{-1}
10	221.55	0.040085	2983.6	8.26×10^6
15	221.55	0.040085	4475.4	1.24×10^7
20	221.55	0.040085	5967.2	1.65×10^7

Firstly, the irrelevance of the computational grid is verified by comparing three different sets of grids, namely, Grid1: 301 × 401, Grid2: 501 × 701, and Grid3: 651 × 1051, and the height of the first layer is not more than 0.001 mm. The calculation conditions are based on the parameters of the Ma = 10 example in Tab. 1. The streamwise velocity and modal growth rate distributions at the middle of the effective computational domain x/L_{ref} = 450 are given Fig. 5. It can be seen that the streamwise velocity and growth rate distribution of Grid1 are different from those of Grid2 and Grid3. Considering the calculation accuracy and time cost, Grid2 grid is used for subsequent calculation.

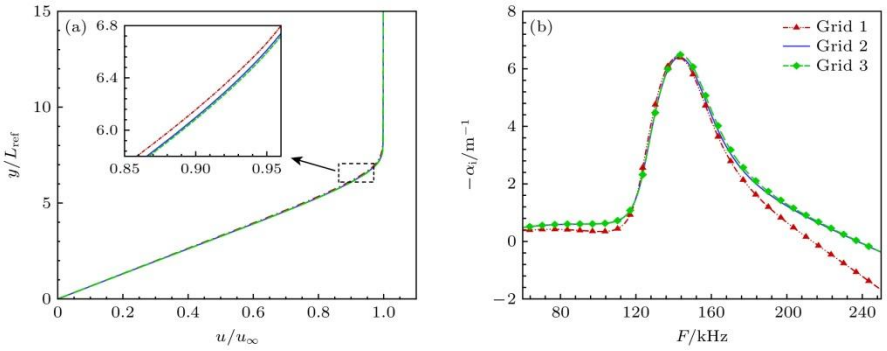

Figure 5. Verification of grid independence: (a) Streamwise velocity; (b) growth rate.

3. Results and Discussion

3.1 Choice of pore model and its effect on flow stability

The influence of pore effect on Mack mode is studied by using the sound absorption characteristics of porous wall. Firstly, based on the two porous models given in the 2.3 section, the influence differences of different wall pore models are explored, and the selected key parameters are half-width (or radius) b = 0. 945 mm, pore depth H = 6. 752 mm, and porosity n = 0. 66. Taking the Ma10 condition under the assumption of calorimetric perfect gas as an example, the x/L_{ref} = 400 position growth rate comparison calculated by the two porous models is given in Fig. 6. Although the growth rate distributions differ significantly between the two porous models, both effectively suppress unstable modes.

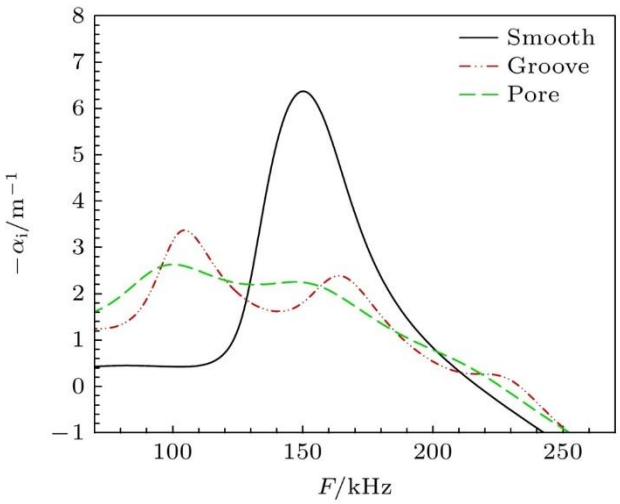

Figure 6. Comparison of growth rate at position x/L_{ref} = 400 for Ma10 condition under CPG.

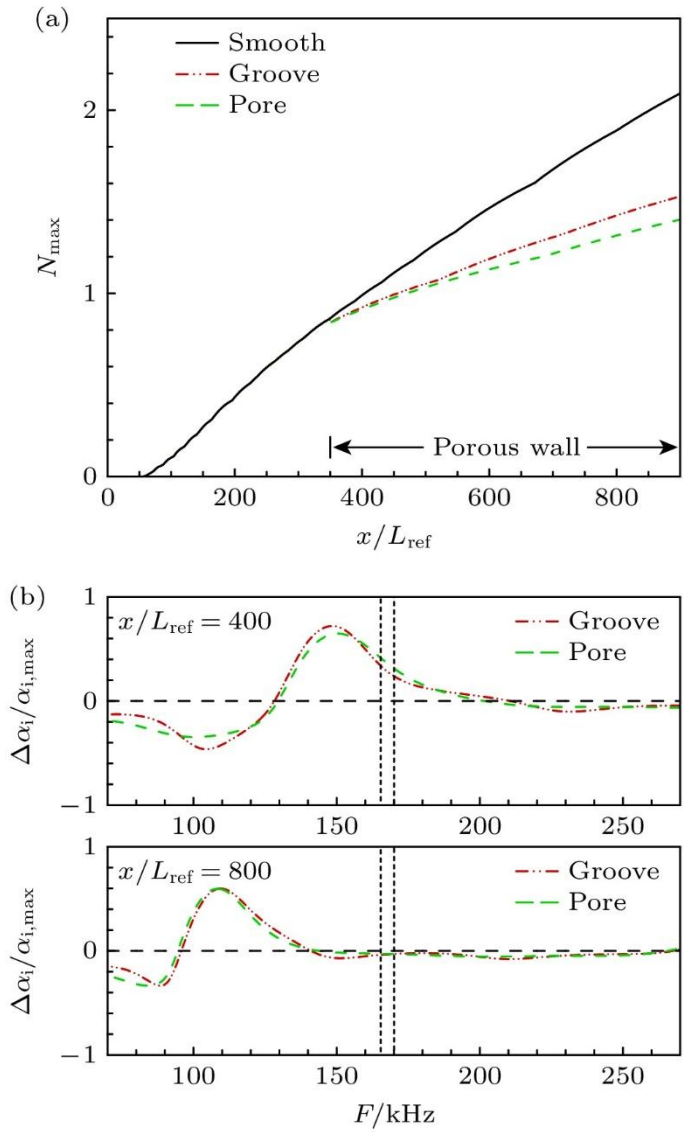

Figure 7. Comparison of results between microgrooves and micropores: (a) *N*-value curves; (b) relative change of growth rate.

To further analyze the difference, Fig. 7 presents the *N* value curve and the $((-\alpha_{\mathrm{i,smooth}} + \alpha_{\mathrm{i,porous}})/\alpha_{\mathrm{i,max}})_{\mathrm{groove/pore}}$ curve of the relative rate of modal growth rate calculated based on the microgroove and micropores models. Compared with the smooth wall, it can be seen that the micropores and microgrooves have a significant effect on suppressing the instability of the boundary layer, and the maximum *N* at the outlet of the flat plate is significantly reduced. Although Fig. 6 show that the growth rates of regular micropores and microgrooves are different, the trend of their relative growth rates shows that different shapes of holes have similar acoustic characteristics. In addition, the maximum *N* value corresponding to the micropores is slightly smaller than that of the microgroove, which is due to the increase of the dominant frequency corresponding to the maximum *N* value under the porous wall (located in the frequency range of the dotted line in Fig. 7(b)). At this dominant frequency, there is $\Delta\alpha_{\mathrm{nom,\ pore}} > \Delta\alpha_{\mathrm{nom,\ groove}}$ in the front part of

the plate. From the peak value of the change rate curve at the position of x/L_{ref} = 400, the microgroove has a better suppression effect on the most. In general, the difference of inhibitory capability between the two is relatively small, and the microgroove model is selected in the subsequent analysis.

In order to explore the influence of microporosity effect on Mack's first and second modes under different microgroove parameters, the parameters of different literatures are selected, as listed in Tab. 2. The variation of modal growth rate with frequency for different wall parameters under Ma10 condition using LST with CPG assumption considering microporosity effect is shown in Fig. 8. It can be seen that Porous-1—3 has a significant inhibitory effect on the second mode, but at the same time it also enhances the first mode. Porous-4 inhibits the first mode, and the maximum growth rate of the second mode is basically unchanged, but its corresponding frequency moves to low frequency. Comparing the effects of the first three profile parameters, it can be seen that Porous-1 has a stronger suppression effect on the second mode in the frequency range of F = 113.7 — 145.6 kHz, but it will make the second mode change from a single peak to an obvious multi-peak. Since the second mode is generally the dominant mode under high Mach conditions, the parameters of Porous-1 are selected for further analysis.

Table 2. Parameters of different cross-sections.

Parameters of porous wall	H/mm	b/mm	n
Porous-1[29]	6.752	0.945	0.66
Porous-2[47]	18.855	0.942	0.66
Porous-3[48]	2.000	0.09375	0.25
Porous-4[52]	0.352	0.264	0.53

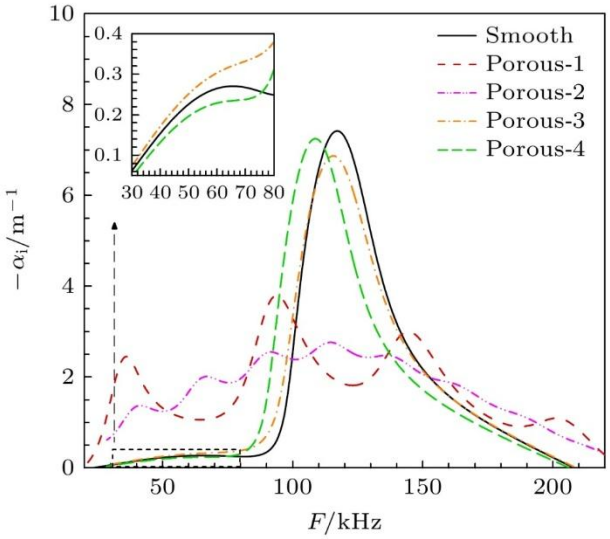

Figure 8. Changes in growth rate under different cross-sectional parameters at x/L_{ref} = 600.

3.2 Chemical non-equilibrium and porous effect on stability

The chemical non-equilibrium effect can affect the characteristics of the basic flow profile, and then affect the instability characteristics of the boundary layer. Firstly, taking the streamwise position x/L_{ref} = 600 in Ma10 condition as an example, the velocity and temperature profiles of different gas models are compared. In Fig. 9, the boundary layer thickness of 8.64 mm (corresponding to 99.5% of the boundary layer edge velocity) at this position in the calorimetrically perfect gas is used as the dimensionless length. It can be seen from the velocity profile that the thickness of the boundary layer decreases when the chemical non-equilibrium effect is considered. From the normal distribution of temperature, it can be seen that the wall temperature in chemical non-equilibrium flow is significantly lower than that in calorimetric perfect gas due to heat absorption of chemical reaction, and the wall temperature difference between them is 481 K under Ma10 condition. It can be seen that in order to accurately simulate the flow, it is necessary to consider the high temperature gas effect under high Mach conditions.

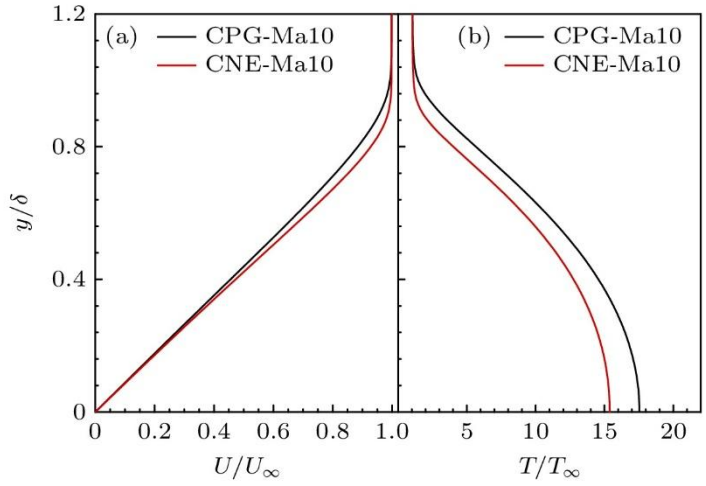

Figure 9. Basic flow profiles of boundary layer for different gas models under Ma10 condition: (a) Streamwise velocity; (b) temperature.

From the above analysis, it can be seen that the existence of chemical reaction significantly changes the basic flow profile, and the disturbance development in the boundary layer is bound to change. Linear stability theory (LST) code is used to calculate the disturbance characteristics in the boundary layer. Firstly, the influence of chemical non-equilibrium effect is studied based on Ma10 condition, and Fig. 10(a) shows the variation of modal growth rate with frequency and the corresponding variation of phase velocity for different gas models at streamwise position x/L_{ref} = 600, where frequency $F = \omega_r \frac{u_e}{2\pi} L_{ref}^{-1}$, phase velocity $C_r = \omega_r/\alpha_r$, α_r and ω_r are the real part of streamwise wavenumber and the real part of circular frequency.

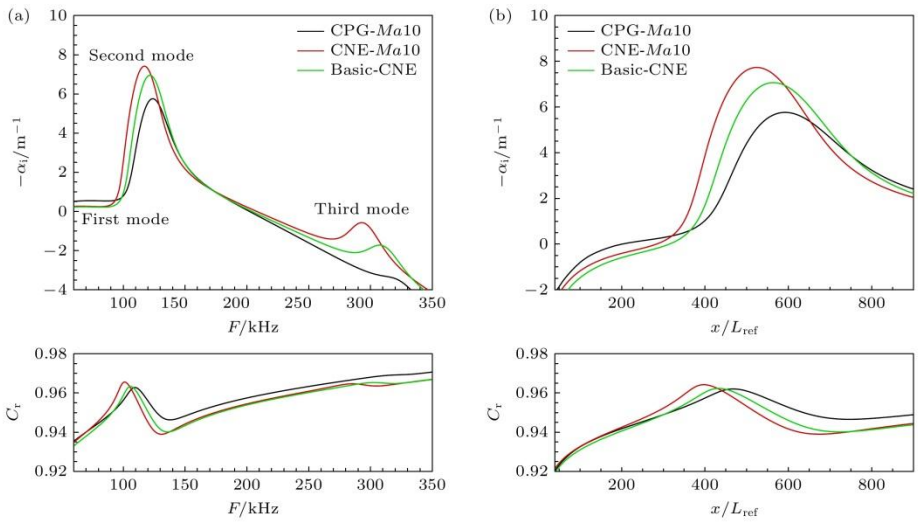

Figure 10. Comparison of growth rate and phase velocity of different gas models under Ma10: (a) x/L_{ref} = 600; (b) modal frequency F = 124 kHz along the streamwise direction.

Fig. 10(a) shows results for calorically perfect gas (CPG), chemical non-equilibrium (CNE), and basic-flow only (Basic-CNE). From Fig. 10(a), it can be seen that the first mode is suppressed, the second mode is promoted, and the third mode is excited when the chemical non-equilibrium effect is considered. The frequencies corresponding to the maximum growth rates of the second and third modes are reduced, and the peak values of their modal phase velocities move to lower frequencies. In addition, when the chemical non-equilibrium effect is considered only in the basic flow and not in the stability equation, the results of the second mode are close to CNE, but between CPG and CNE. Comparing the above three cases, the main reason for the suppression of the first mode is the influence of the chemical non-equilibrium effect on the basic flow. The variation of the growth rate of the disturbance with frequency F = 124 kHz along the streamwise direction and the corresponding phase velocity are given in Fig. 10(b) for different gas models. For the same frequency disturbance in the flow, the chemical non-equilibrium effect makes the second mode growth rate and mode phase velocity reach the peak value faster.

In order to discuss the influence of chemical non-equilibrium effect on modal stability more intuitively, Fig. 11(a) gives the neutral curve distribution of the first mode and the second mode under different gas models. In the front region of the plate, the chemical non-equilibrium effect makes the unstable second mode extend to the high frequency region, and the high frequency disturbance is excited earlier. The lower branch of the neutral curve of the second mode also shows that its unstable frequency moves slightly to low frequency, and the unstable frequency range of the second mode increases as a whole. For the first mode, the chemical non-equilibrium effect acts as a suppression, and its unstable frequency range is reduced. However, the calculation result of only considering the chemical non-equilibrium effect in the basic flow is not between the CPG

and CNE as the second mode, but is further downstream than the neutral curve of CNE, which indicates that the chemical non-equilibrium effect in the basic flow is inhibitory to the first mode, but the chemical non-equilibrium effect in the perturbation stability equation is promoting, and the inhibitory effect of the former is greater than that of the latter. By comparing the *N* envelopes of the three cases in Fig. 11(b), it can be seen that the chemical non-equilibrium effect in the basic flow and stability equations will increase the maximum *N* and promote the instability of the boundary layer.

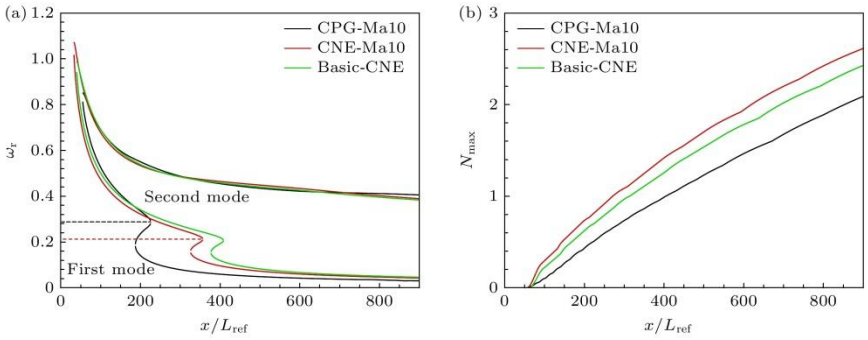

Figure 11. Comparison of different gas models under Ma10: (a) Neutral curves; (b) *N*-value envelope.

In general, the influence of high temperature chemical non-equilibrium effect on modal stability is mainly through the influence on basic flow, but the influence of this effect on stability equation can not be ignored from the point of view of scientific research, and trade-offs may be considered in engineering application for efficiency.

For the study considering the coexistence of chemical non-equilibrium and micropore effect, the Mach 10 condition is selected to compare the modal growth rates of different gas models with the same wall parameters, and Fig. 12 gives the comparison of growth rates and their relative rates $((-\alpha_{\mathrm{i,smooth}} + \alpha_{\mathrm{i,porous}})/\alpha_{\mathrm{i,max}})$ at positions x/L_{ref} = 400, 600 and 800. It can be seen from Fig. 12(a) that the porous wall makes the first mode more unstable under different gas models, but the second mode is obviously suppressed. Compared with the relative change rate curve, in the second modal frequency range, the suppression effect of porous wall in CNE condition is first greater than that in CPG condition, and then less than that in CPG condition with the increase of frequency, which indicates that the chemical non-equilibrium effect reduces the modal frequency range in which the porous effect plays a suppression role. This phenomenon causes the chemical non-equilibrium effect to enhance the suppression of the microporosity effect in the local low frequency range (between the two dotted lines) and to weaken in most other frequency ranges (the region to the right of the second dotted line). In addition, the influence of chemical non-equilibrium effect is not obvious from the peak value of relative change rate. By comparing the results of different positions, the dominant frequency of the

unstable mode decreases with the increase of the streamwise position, the relative change trend of the growth rate in Fig. 12(b) and Fig. 12(c) is the same as that in Fig. 12(a), and the corresponding frequency range of $\Delta\alpha_{nom,\ CNE} > \Delta\alpha_{nom,\ CPG}$ also decreases with the increase of the streamwise position.

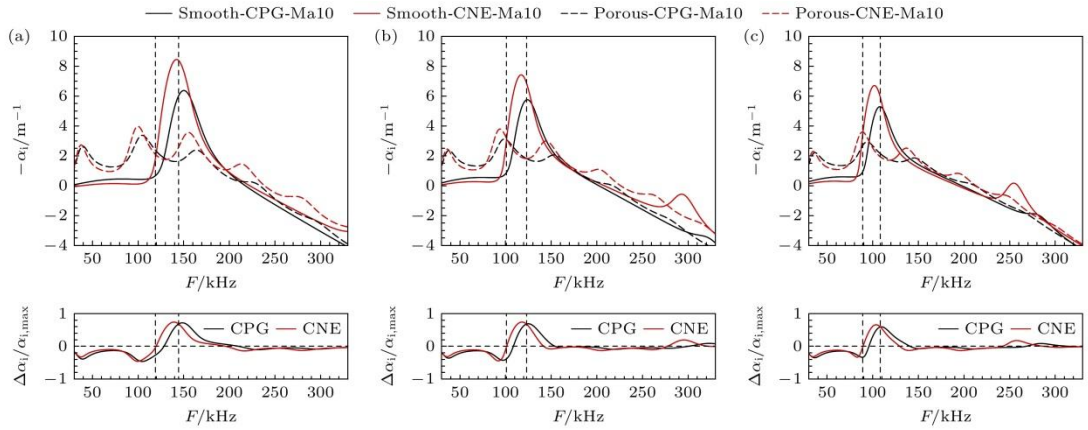

Figure 12. Comparing the growth rates of smooth and porous walls and their relative change for different gas models: (a) x/L_{ref} = 400; (b) x/L_{ref} = 600; (c) x/L_{ref} = 800.

In order to analyze the influence of surface micropore effect on the eigenfunctions of disturbance, the characteristic solution corresponding to the frequency F = 124 kHz is taken, and the corresponding pressure characteristic function amplitude distribution is shown in Fig. 13. The black and red horizontal dotted lines in the figure represent the edge of the boundary layer at the streamwise position x/L_{ref} = 600 for CPG and CNE conditions, respectively. It can be seen from Fig. 13 that the eigenfunctions of CNE and CPG are basically the same, but the disturbance amplitude in the near-wall region is significantly reduced under the influence of the micropore effect, and the normal position corresponding to the peak pressure disturbance changes from the near-wall region to the region near the outer edge of the boundary layer.

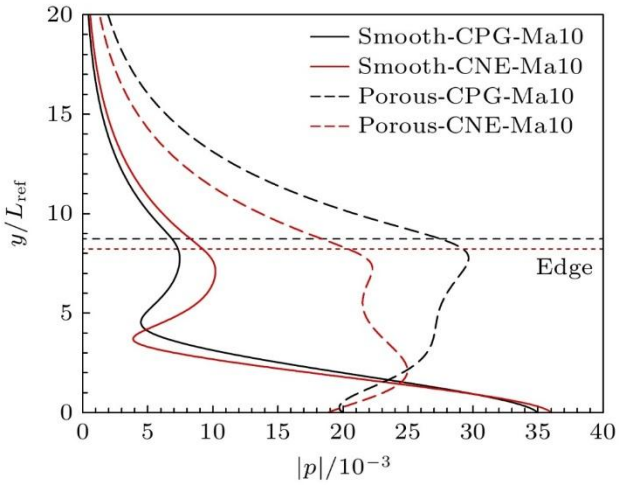

Figure 13. Comparison of the pressure eigenfunctions for smooth and porous walls at x/L_{ref} = 600.

According to the existing research[32], the presence of a porous wall at the leading edge of a flat plate will excite unstable modes and increase the N. Therefore, in order to investigate the inhibition effect of micropores, the porous wall is set at the streamwise position x/L_{ref} = 350, and the N value curves of smooth and porous walls under the two gas models are further compared, as shown in Fig. 14. The micropore effect under different gas models can reduce the maximum N value, which is reduced by 26. 83% under CPG condition and 18. 22% under CNE condition. The difference between the two conditions is mainly due to the increase of the frequency corresponding to the maximum N value under the porous wall, which is 155 kHz and 165 kHz, respectively. According to Fig. 12, the corresponding frequency is $\Delta\alpha_{nom,\,CNE}<\Delta\alpha_{nom,\,CPG}$. This shows that the pore effect significantly delays instability under the two gas models, but the chemical non-equilibrium effect weakens the effect of pore, which is contrary to the conclusion of Wang[40]. The reason is that Wang's work only examined single-frequency results at 300 and 400 kHz, which is not a substitute for evaluating the overall effect of a wide frequency range. In addition, by comparing the red dotted line and the black solid line, it can be found that the N value considering both the chemical non-equilibrium and the pore effect is larger than that not considering both, which indicates that the chemical non-equilibrium effect has a stronger promoting effect on the mode than the pore effect, resulting in the overall coexistence of the two effects is to promote instability.

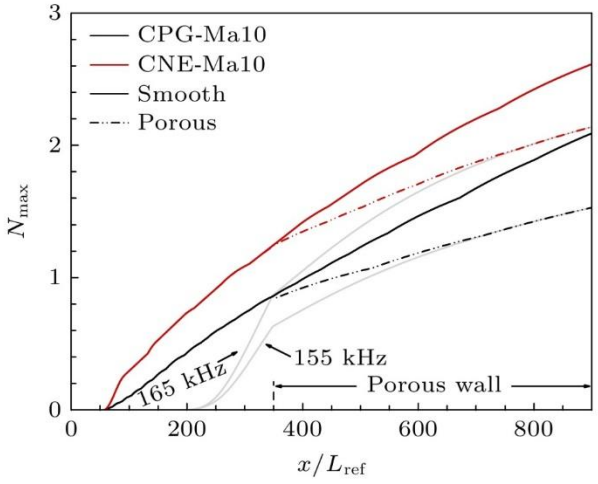

Figure 14. Comparison of N-value envelope for smooth and porous walls of different gas models.

3.3 Mach number effect on that stability of chemical nonequilibrium flow

In calorimetrically perfect gas flow, the increase of Mach number will lead to a more stable boundary layer and a delayed transition position[1]. Conditions at Mach numbers 10, 15, and 20 are examined to analyze the effect of Mach number on unstable modes in chemical nonequilibrium flow. First, the stability of chemical non-equilibrium flow at

different Mach numbers under smooth wall conditions is compared, and the growth rate comparison of different Mach numbers at streamwise position x/L_{ref} = 600 is shown in Fig. 15(a). It can be seen from Fig. 15(a) that with the increase of Mach number, the disturbances of the first and second modes are suppressed, the peak value of the growth rate decreases, and the corresponding frequency has little effect. In addition, with the increase of Mach number, the third mode disturbance is excited and gradually becomes unstable, but the second mode is still dominant. Further, the variation of the disturbance growth rate along the streamwise direction for the second mode F = 130 kHz is given in Fig. 15(b). With the increase of the Mach number, the peak value of the mode growth rate decreases, but the position of the most unstable growth rate is similar, which means that the Mach number influences the rate at which the mode grows.

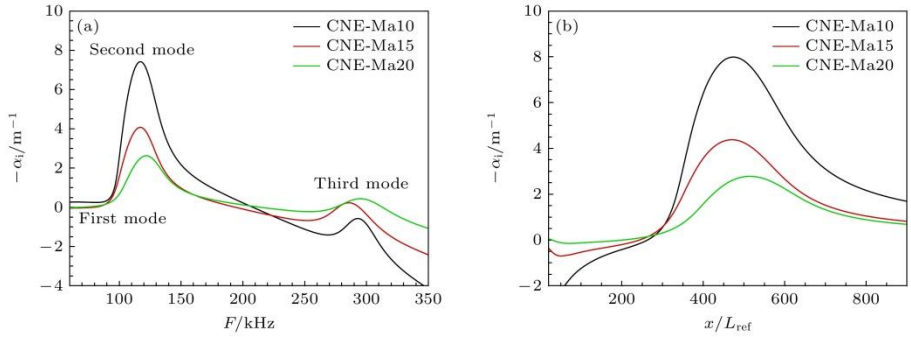

Figure 15. Comparison of growth rates at different Mach numbers under CNE condition: (a) x/L_{ref} = 600; (b) modal frequency F = 130 kHz along the streamwise direction

Similarly, the boundary layer neutral curves at different Mach numbers are given in Fig. 16, the results of the chemical non-equilibrium gas model are given in Fig. 16(b), and the results of the calorimetric perfect gas model are given in Fig. 16(a) for comparison. It can be seen from Fig. 16(a) that as the Mach number increases, the unstable frequencies of the first and second modes of the boundary layer move to lower frequencies, and the streamwise location where the low-frequency disturbance begins to lose stability moves upstream. At the same time, the first and second modes are connected downstream, and there is no neutral point in the connected frequency range. For the chemical non-equilibrium gas model, the influence of the Mach number is relatively complex. In Fig. 16(b), there are the first mode and the second mode of instability in the Ma10 boundary layer, and their unstable regions are connected downstream. There is only an unstable second mode in the Ma15 boundary layer, and the first mode becomes stable. In addition to the unstable second mode, there is also an unstable third mode in the Ma20 boundary layer, which is connected to the second mode downstream.

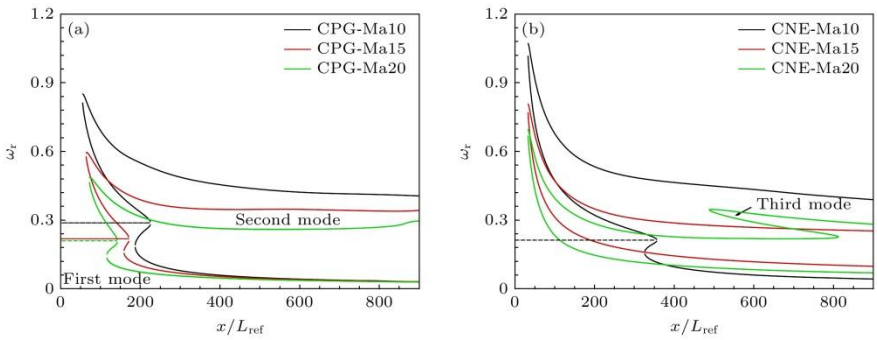

Figure 16. Comparison of neutral curves at different Mach numbers: (a) CPG; (b) CNE.

Fig. 17 shows the envelope of *N*-value at different Mach numbers, and the single-frequency *N* curve corresponding to the modal frequency of 130 kHz. It can be seen that with the increase of Mach number, the *N* value decreases, but the modal frequency corresponding to the maximum *N* value is similar, which indicates that Mach number has an inhibitory effect on the instability of chemical non-equilibrium boundary layer.

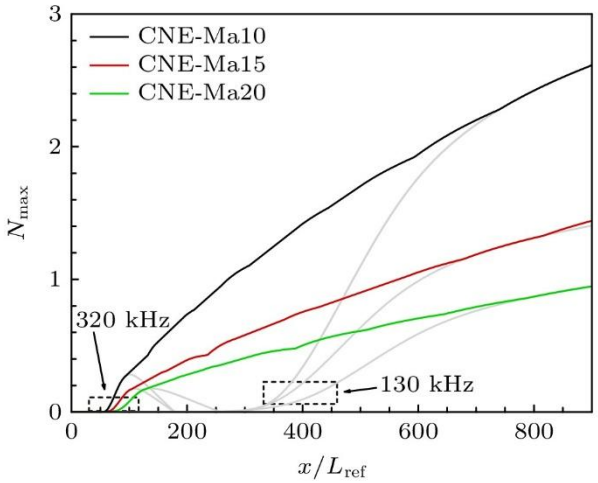

Figure 17. Comparison of *N*-value envelopes at different Mach numbers under CNE condition.

The effect of the Mach number on the stability of chemical non-equilibrium boundary layer under the condition of porous wall is analyzed below. Fig. 18 gives the modal growth rate and its relative rate of change at streamwise positions x/L_{ref} = 400 and 600 for different Mach number conditions and compares them with those of smooth wall. According to Fig. 18(a), it can be seen that the first and second modes of the porous wall boundary layer can also be suppressed by increasing the Mach number. Compared with the smooth wall, the influence of the porous effect on the boundary layer mode decreases with the increase of Mach number. From the position of x/L_{ref} = 400, the larger the Mach number is, the weaker the excitation effect of the first mode is, but the suppression effect of the second mode is basically unchanged. The frequency corresponding to the most

significant suppression effect of the porous wall is basically close to the frequency corresponding to the maximum instability growth rate. The same trend is seen at the downstream x/L_{ref} = 600 location.

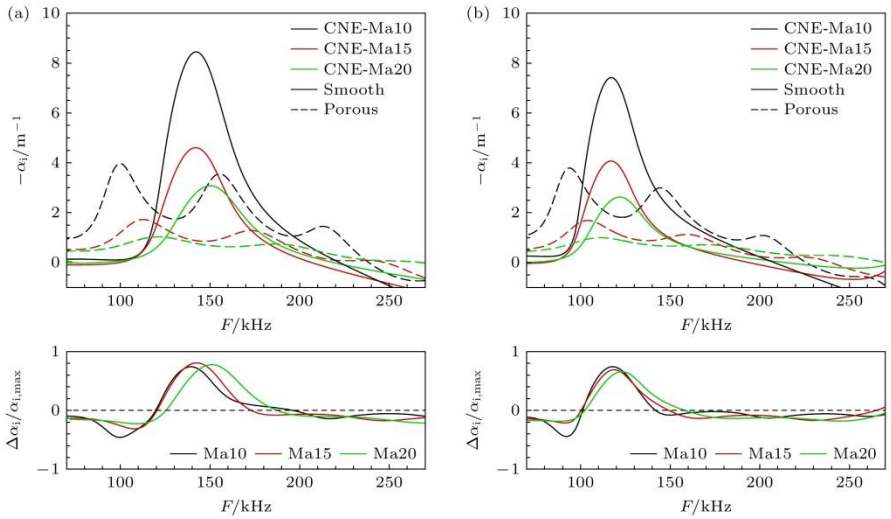

Figure 18. Comparison of growth rates and relative change of smooth and porous walls at different Mach numbers: (a) x/L_{ref} = 400; (b) x/L_{ref} = 600.

Fig. 19 gives the envelope of *N*-values for chemical nonequilibrium flow over smooth and porous walls. It can be seen from Fig. 19 that the porous wall can effectively reduce the *N* value at different Mach numbers, but the dominant frequency corresponding to the maximum *N* value increases with the increase of Mach number. Table 3 lists the relative change in N-value ($\Delta N/N_{max,\ smooth}$) at the outlet position x/L_{ref} = 900 for both gas models at different Mach numbers, and the overall suppression effect of pore effect on boundary layer instability under different working conditions is analyzed. In the studied Mach number range, the relative reduction of the CPG condition is greater than that of the CNE condition, which indicates that the suppression effect of chemical non-equilibrium effect on porous wall is weakened at different Mach numbers.

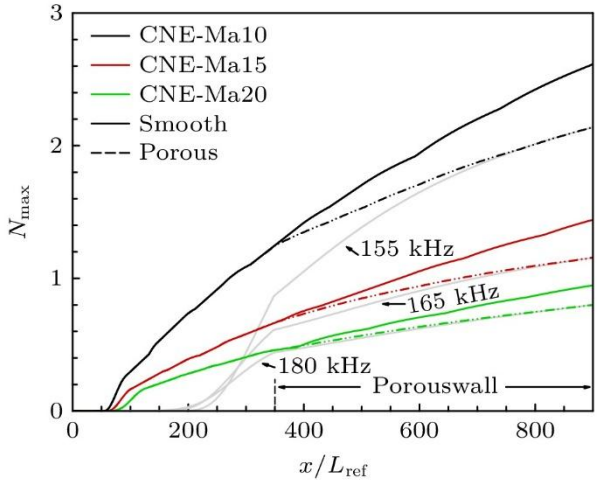

Figure 19. *N*-value envelopes of smooth and porous walls at different Mach numbers.

Table 3. Relative change of N-values at x/L_{ref} = 900 under different Mach numbers.

Ma	$(\Delta N/N_{max,\ smooth})_{CPG}$	$(\Delta N/N_{max,\ smooth})_{CNE}$
10	26.8%	18.2%
15	22.1%	19.8%
20	27.2%	15.5%

4. Conclusion

In this paper, a linear stability analysis method (LST) is established to study the effects of chemical non-equilibrium, surface micropore effect, and Mach number on the instability of high enthalpy boundary layer flow at high Mach number (H = 25 km), in which the chemical non-equilibrium and microporosity effects coexist. The main conclusions are as follows:

1) The chemical non-equilibrium effect can promote the second mode, suppress the first mode, and excite the third mode, but the second mode is always dominant in general, thus promoting the instability of the boundary layer. Although the overall effect of chemical non-equilibrium on the first mode is suppression, the chemical non-equilibrium effect in the stability equation is promotion, and the suppression of the first mode is mainly due to the change of the basic flow. Therefore, from the point of view of scientific research, the consideration of chemical non-equilibrium effects on the stability equation can not be ignored.

2) When the micropore effect is further considered in the chemical nonequilibrium flow, the micropore effect can promote the first mode and inhibit the second mode, and the instability is inhibited on the whole. The effect of the microporosity effect is roughly opposite to that of the chemical nonequilibrium effect, and the inhibitory effect of the former on the second mode is weaker than the promoting effect of the latter, which leads to the instability being promoted on the whole when the two effects coexist compared with the smooth wall condition under the calorimetric perfect gas model. Compared with the pore effect of the calorimetric perfect gas model, the chemical non-equilibrium effect reduces the frequency range corresponding to the second mode of pore effect suppression, resulting in the ability of the pore effect to suppress instability in the local low frequency range but weakens in other second mode instability regions, resulting in the reduction of the N value caused by pore effect.

3) In chemical nonequilibrium flow, with the increase of Mach number, the first and second modes are suppressed, the third mode is excited and gradually unstable, and the corresponding frequencies of the peak growth rate are similar, which leads to the decrease of the maximum *N* value, but the dominant frequencies are similar. If the micropore effect is considered, the excitation of the first mode by the porous wall will be weakened with the increase of the Mach number, and the suppression of the second mode will not be affected. In the investigated Mach number range (10-20), the microporosity effect can still effectively suppress the instability, but compared with the calorimetric perfect gas condition without considering the microporosity effect, the effect of the coexistence of the two effects is to promote.

This paper is strongly supported by the NNW-HyFLOW team of the Institute of Computational Aerodynamics, China Aerodynamics Research and Development Center, and the help of Zhang Bin, Li Xiaohu, Gong Geng, etc., of the National Key Laboratory of Aerospace Flight Aerodynamics Science and Technology. We would like to express our gratitude here.

References

[1] Chen J Q, Tu G H, Zhang Y F, Xu G L, Yuan X X, Chen C 2017 *Acta Aerodyn. Sin.* **35** 311

[2] Currie J G, Dickason A M 1988 *Report of the Defense Science Board Task Force on the National Aerospace Plane （NASP）* Report No. AD-A201 124

[3] Candler G V 2019 *Annu. Rev. Fluid Mech* **51** 379

[4] Bitter N P 2015 *Ph. D. Dissertation* （Pasadena: California Institute of Technology

[5] Malik M R 1991 *Phys. Fluids* **3** 803

[6] Stuckert G, Reed H L 1994 *AIAA J.* **32** 1384

[7] Hudson M L, Chokani N, Candler G V 1997 *AIAA J.* **35** 958

[8] Franko K, Maccormack R, Lele S 2010 *40th Fluid Dynamics Conference and Exhibit* Chicago, June 28–July 1, 2010 p4601

[9] Chen X L, Wang L, Fu S 2021 *Phys. Fluids* **33** 034132

[10] Zhao Z Y, Chen X L, Wang L, Fu S 2023 *Phys. Gases* **8** 35

[11] Li C H, Wan B B, Tu G H, Hu W B, Chen J Q, Jiang C W 2024 *Acta Aerodyn. Sin.* **42** 12

[12] Fernando M M, Beyak E S, Pinna F, Reed H L, Brussels B 2019 *Phys. Fluids* **31** 044101

[13] Mcbride B J, Zehe M J, Sanford G 2002 *NASA Glenn Coefficients for Calculating Thermodynamic Properties of Individual Species* （National Aeronautics and

Space Administration Glenn Research Center） Report No. NASA/TP-2002-211556

[14] Magin T, Degrez G 2005 *J. Comput. Phys.* **198** 424

[15] Yos J M 1963 *Transport Properties of Nitrogen, Hydrogen, Oxygen and Air to 30000 K*（Research & Advanced Development Division Avco Corporation Technical Memorandum） Report No. AD-435 053

[16] Ramshaw J D 1993 *J. Non-Equilibrium Thermodyn.* **18** 12

[17] Chapman S, Cowling T G 1952 *Math. Gaz.* **38** 323

[18] Blottner F G, Johnson M, Ellis M 1971 *Chemically Reacting Viscous Flow Program for Multi-component Gas Mixtures* Report No. SC-RR-70-754

[19] Brokaw R S 1965 *J. Chem. Phys.* **42** 1140

[20] Gupta R N, Yos J M, Thompson R A 1990 *A Review of Reaction Rates and Thermodynamic and Transport Properties for the 11-species Air Model for Chemical and Thermal Nonequilibrium Calculations to 30000 K*（National Aeronautics and Space Administration Langley Research Center） Report No. NASA-TM-101528

[21] Wan B B, Han Y F, Fan Y, Luo J S 2017 *J. Aerosp. Power* **32** 188

[22] Park C, Jaffe R L, Partridge H 2001 *J. Thermophys. Heat Transfer* **15** 76

[23] Park C 1985 *AIAA 23rd Aerospace Sciences Meeting*, Reno, Nevada, January 14–17, 1985 p85–0247

[24] PARK C 1993 *J. Thermophys. Heat Transfer* **7** 385

[25] Li C H, Wan B B, Chen J Q, Tu G H, Hu W B, Jiang C W 2024 *Int. J. Heat Mass Transfer* **233** 126018

[26] Al-Jothery H K M, Albarody T M B, Yusoff P S M, Abdullah M A, Hussein A R 2020 *IOP Conference Series: Materials Science and Engineering* **863** 012003

[27] Malmuth N, Fedorov A, Shalaev V, Cole J, Khokhlov A, Hites M, Williams D 1998 *2nd AIAA Theoretical Fluid Mechanics Meeting*, Albuquerque, New Mexico, June 15–18, 1998 p2695

[28] Fedorov A, Malmuth N, Rasheed A, Hornung H G 2001 *AIAA J.* **39** 605

[29] Zhao R, Liu T, Wen C Y, Zhu J, Cheng L 2018 *AIAA J.* **56** 2942

[30] Wartemann V, Heinrich L, Sandham N D 2009 *16th AIAA/DLR/DGLR International Space Planes and Hypersonic Systems and Technologies Conference*, Bremen, Germany, October 19–22, 2009 AIAA 2009-7202

[31] Xu J K, Liu J X, Mughal S, Yu P X, Bai J Q 2020 *Phys. Fluids* **32** 044105

[32] Wang X Q, Zhong X L 2012 *Phys. Fluids* **24** 034105

[33] Rasheed A, Hornung H G, Fedorov A, Malmuth N D 2002 *AIAA J.* **40** 481

[34] Lukashevich S V, Morozov S O, Shiplyuk A N 2016 *J. Appl. Mech. Tech. Phys.*

57 873

[35] Guo Q L, Tu G H, Chen J Q, Yuan X X, Wan B B 2020 *J. Aerosp. Power* **35** 135

[36] Liu Y, Tu G H, Xiang X H, Li X H, Guo Q L, Wan B B 2022 *Acta Phys. Sin.* **71** 194701

[37] Gui Y T, Wang W Z, Zhao R, Zhao J Q, Wu J 2022 *AIAA J.* **60** 4453

[38] Liu X, Zhao R, Wen C Y, Yuan W 2024 *Acta Mech.* **235** 1109

[39] Wang X W, Zhong X L 2013 *51st AIAA Aerospace Sciences Meeting including the New Horizons Forum and Aerospace Exposition* Grapevine, Texas, January 7–10, 2013 p827

[40] Wang X W 2018 *AIAA Aerospace Sciences Meeting* Kissimmee, Florida, January 8–12, 2018 p2088

[41] Ken C K U, Hao J, Zhao R, Wen C Y 2023 *Aerosp. Sci. Technol.* **141** 108520

[42] Walter G V, Charles H K, Teichmann T 1966 *Phys. Today* **19** 95

[43] Bird R B, Stewart W E, Lightfoot E N 2002 *Appl. Mech. Rev.* **55** R1

[44] Wilke C R 1950 *J. Chem. Phys.* **18** 517

[45] Wan B B, Su C H, Chen J Q 2020 *AIAA J.* **58** 4047

[46] Zhao R, Wen C Y, Tian X D, Long T H, Yuan W 2018 *Int. J. Heat Mass Transfer* **121** 986

[47] Brès G A, Inkman M, Colonius T, Fedorov A 2013 *J. Fluid Mech* **726** 312

[48] Luedeke H, Sandham N D, Wartemann V 2012 *AIAA J.* **50** 1281

[49] Zhao R, Zhang X X, Wei H G, Wen C Y 2021 China Patent CN110135062B [2021-10-29]

[50] Kline H L, Chang C L, Li F 2018 *Fluid Dynamics Conference* Atlanta, Georgia, June 25–29, 2018 p3699

[51] Miró M Fernando, Pinna F, Beyak E S, Barbante P, Reed H L 2018 *AIAA Aerospace Sciences Meeting* Kissimmee, Florida, January 8–12, 2018 p1824

[52] Zhao R, Yan H, Xi K, Wen C Y 2020 *Aeronaut. Sci. Technol.* **31** 104